2-1-2005

Characteristics of Instabilities in the Mesopause Region over Maui, Hawaii

Feng Li
University of Illinois at Urbana-Champaign

Alan Z. Liu
Embry Riddle Aeronautical University - Daytona Beach, liuz2@erau.edu

Gary R. Swenson
University of Illinois at Urbana-Champaign

Characteristics of instabilities in the mesopause region over Maui, Hawaii

Feng Li

Department of Atmospheric Sciences, University of Illinois at Urbana-Champaign, Urbana, Illinois, USA

Alan Z. Liu and Gary R. Swenson

Department of Electrical and Computer Engineering, University of Illinois at Urbana-Champaign, Urbana, Illinois, USA

Received 4 June 2004; revised 14 November 2004; accepted 8 December 2004; published 1 February 2005.

[1] Characteristics of convective and dynamical instabilities in the mesopause region (between 85 and 100 km) over Maui, Hawaii (20.7°N, 156.3°W) are investigated using 19 nights, ~133 hours of high-resolution wind and temperature data obtained by the University of Illinois Na wind/temperature lidar during the Maui Mesosphere and Lower Thermosphere (Maui MALT) campaigns. The mean probabilities of convective and dynamical instabilities are observed to be ~3 and 10%, respectively, but there is considerable night-to-night variation. At any given time the probability that an unstable condition is found at some altitudes in the 85–100 km range is ~90%. The Maui MALT data exhibit a distinct trend for N^2 to increase with wind shear and vice versa. This correlation has important implications in the understanding of the development of instabilities. The night of 11 April 2002 is studied in detail in order to investigate the spatial and temporal structures of N^2, wind shear, and convective and dynamical instabilities. A close linkage between instability and the mesosphere inversion layers (MILs) is identified. Most of the convectively and dynamically unstable regions are located above the MILs, with a tendency for dynamical instability to develop below convective instability. It is found that the vertical variations of N^2 are often correlated with those of wind shear, but with a phase shift such that the maxima and minima of N^2 are located ~0.5–1 km below those of wind shear. Because of this shift, dynamical instability tends to develop in the region above the maximum wind shear, where relatively small N^2 is observed to be associated with large wind shear. We also found that the wind shear is dominated by the contribution of the meridional wind, especially when the wind shear is strong. Possible mechanisms for the observed features are discussed.

Citation: Li, F., A. Z. Liu, and G. R. Swenson (2005), Characteristics of instabilities in the mesopause region over Maui, Hawaii, *J. Geophys. Res.*, *110*, D09S12, doi:10.1029/2004JD005097.

1. Introduction

[2] It is now widely accepted that gravity waves play an essential role in determining the large-scale circulation in the mesosphere and lower thermosphere (MLT). Gravity waves achieve large amplitudes and break when propagating into the MLT from the lower atmosphere. Breaking waves generate turbulence and significantly influence the wind, temperature, and composition structures in this region. Convective and dynamical instabilities are dominant mechanisms for gravity wave breaking. Early theoretical studies have investigated the roles of instabilities in gravity wave dissipation and turbulence generation [e.g., *Hodges*, 1967; *Lindzen*, 1981; *Fritts and Rastogi*, 1985; *Fritts and Yuan*, 1989]. Recent theoretical and numerical studies have greatly improved the understanding of gravity wave instability dynamics [e.g., *Andreassen et al.*, 1994, 1998; *Fritts et al.*, 1994, 1998; *Isler et al.*, 1994; *Lombard and Riley*, 1996; *Sonmor and Klaassen*, 1997; *LeLong and Dunkerton*, 1998a, 1998b; *Liu et al.*, 1999].

[3] Numerous observations of instability structures and gravity wave breaking in the MLT have been reported in the mesopause region (in the height range of ~80 and 105 km) in recent years. Small-scale ripples, which are believed to be manifestations of instabilities, are frequently observed in the mesopause airglow image data [e.g., *Taylor and Hapgood*, 1990; *Taylor et al.*, 1997; *Nakamura et al.*, 1999; *Hecht*, 2004]. Overturning of sodium (Na) mixing ratio is commonly observed in the mesopause region by Na lidar [e.g., *Williams et al.*, 2002; *Liu et al.*, 2004]. Because Na mixing ratio is a good tracer of wave motion [*Clemesha et al.*, 1982; *Hickey and Plane*, 1995], overturning in Na mixing ratio indicates similar overturning in potential temperature and convective instability. Direct observations of gravity wave breaking are primarily made by airglow imagers [e.g., *Swenson and Mende*, 1994; F. Li et al., Observations of gravity wave breakdown into ripples associated with dy-

0148-0227/05/2004JD005097$09.00

namical instabilities, submitted to *Journal of Geophysical Research*, 2004, hereinafter referred to as Li et al., submitted manuscript, 2004]. *Yamada et al.* [2001] reported a particular example of the breakdown of a gravity wave into turbulence in OH airglow. A combination of observational and numerical studies provides possible explanations for the observations. For example, *Fritts et al.* [1997] and *Hecht et al.* [1997] combined a 3-D numerical simulation with correlative observations of airglow images and wind measurements to investigate a ripple event in OH airglow. They suggested that this ripple event is a manifestation of streamwise convective instability.

[4] Because of the importance of instabilities in the MLT, characterizing them will improve our understanding of the dynamics in this region. *Zhao et al.* [2003] (hereinafter referred to as Z03) studied atmospheric stability in the mesopause region at Starfire Optical Range (SOR), near Albuquerque, NM (35.0°N, 106.5°W) using high-resolution Na lidar wind and temperature data collected between June 1998 and October 1999. They focused on seasonal variations of instabilities, and found that the probabilities of both convective and dynamical instabilities have a minimum in summer and a maximum in winter. Semidiurnal tides have significant impacts on the distribution of convectively unstable regions. Tides set up a favorable environment for convective instability to develop above the altitude region of positive temperature gradient associated with the tidal temperature perturbation. They also found that dynamical instability generally occurs before and below convective instability, which they attributed to the phase difference between tidal temperature and wind perturbations.

[5] In this paper, we report the characteristics of instabilities in the mesopause region over Maui, HI (20.7°N, 156.3°W) using Na lidar measurements obtained in the Maui Mesosphere and Lower Thermosphere (Maui MALT) campaigns. The objective of this study is to fully characterize the statistics and structures of convective and dynamical instabilities in this low-latitude site. Totally, 19 nights, ~133 hours of high-resolution wind and temperature data are analyzed. Distinct features, such as the links between instabilities and mesospheric inversion layers, and the consistent correlation of the atmospheric static stability with the vertical shear in horizontal winds, are identified. These features are not studied in Z03, but have important implications in the dynamics in the mesopause region. Possible mechanisms for the observed features are also discussed.

2. Observation and Data Analysis

[6] The University of Illinois Na wind/temperature lidar has been operated in a seasonal campaign mode since January 2002 on Mt. Haleakala on Maui, HI. Details of the instrumentation can be found in the work of *Chu et al.* [2005]. Coupled with a steerable 3.67 m diameter astronomical telescope at the Air Force Maui Optical Station, the lidar system measures the line-of-sight (LOS) Na density, Doppler temperature, and Doppler wind profiles in the 80–105 km height range. Six campaigns were conducted from January 2002 to January 2004. Totally, 24 nights, ~165 hours of data were collected. In a normal operation mode, the lidar is pointed to the zenith (Z), and 30° off the zenith toward north (N), east (E), south (S) and west (W) in ZNEZSW sequence. The horizontal winds are derived from off-zenith LOS wind measurements with the following relationships:

$$V_E = u_E \sin\theta + w\cos\theta, \tag{1a}$$

$$V_W = -u_W \sin\theta + w\cos\theta, \tag{1b}$$

$$V_N = v_N \sin\theta + w\cos\theta, \tag{1c}$$

$$V_S = -v_S \sin\theta + w\cos\theta, \tag{1d}$$

where V is the LOS wind, u is the zonal wind, v is the meridional wind, w is the vertical wind, $\theta = 30°$ is the zenith angle, and the subscripts E, W, N, S denote the lidar beam positions. We calculate the horizontal wind simply as the LOS wind divided by sinθ and ignore the vertical wind. That is,

$$u'_E = V_E/\sin\theta = u_E + w\cot\theta, \tag{2a}$$

$$u'_W = -V_W/\sin\theta = u_W - w\cot\theta, \tag{2b}$$

$$v'_N = V_N/\sin\theta = v_N + w\cot\theta, \tag{2c}$$

$$v'_S = -V_S/\sin\theta = v_N - w\cot\theta, \tag{2d}$$

where the superscript prime denotes an approximation of the real horizontal wind. Among the 24 nights, there are five "zenith" nights when the lidar was pointed to the zenith most of the night. Because both temperature and horizontal winds are needed for instability investigation, the zenith nights are not included in this study. Table 1 summarizes the statistics of the data used in this paper.

[7] The stability of the atmosphere is characterized by the square of Brunt-Vaisala frequency (N^2) and the Richardson number (Ri). N^2 is defined as

$$N^2 = \frac{g}{T}\left(\frac{dT}{dz} + \frac{g}{c_p}\right), \tag{3}$$

and Ri is defined as

$$Ri = \frac{N^2}{S^2}, \tag{4}$$

where T is temperature, g is the acceleration of gravity, c_p is the specific heat at constant pressure, and $S = \sqrt{\left(\frac{du}{dz}\right)^2 + \left(\frac{dv}{dz}\right)^2}$ is the vertical shear in the horizontal winds. Convective instability may occur when $N^2 < 0$. The necessary but not sufficient condition for dynamical instability is $0 < Ri < 1/4$ [*Miles*, 1961]. It should be noted that this traditional view of instabilities may not be complete under all circumstances. Several theoretical and numerical studies have suggested that instabilities may occur outside of these critical limits

Table 1. Nightly and Annual Mean of the Probability of Convective and Dynamical Instabilities, N^2, and Amplitude of Vertical Shear in the Zonal Wind, Meridional Wind, and the Total Horizontal Wind

Date	Time, hours	$P(N^2 < 0)$, %	$P(0 < Ri < 0.25)$, %	N^2, 10^{-4}	S, $ms^{-1}km^{-1}$	$\lvert du/dz \rvert$, $ms^{-1}km^{-1}$	$\lvert dv/dz \rvert$, $ms^{-1}km^{-1}$
01/14/2002	5.25	2.8	14.1	4.21	26.0	14.7	16.2
01/15/2002	10.50	2.8	6.1	3.83	21.4	8.1	14.3
01/20/2004	4.25	1.7	19.4	3.82	28.7	14.6	18.0
01/22/2004	3.00	10.7	10.3	4.76	24.8	11.5	14.2
04/11/2002	9.25	4.2	21.5	4.72	33.4	15.1	22.7
04/13/2002	10.50	1.5	8.1	4.23	21.8	9.7	13.9
04/15/2002	3.00	6.5	25.4	3.15	28.2	16.7	15.0
04/17/2002	5.75	3.2	19.8	4.94	33.7	15.1	22.8
07/07/2002	6.75	4.2	8.7	4.46	27.8	12.1	17.7
07/09/2002	8.00	3.0	7.7	3.82	23.3	9.7	15.3
07/13/2002	5.00	2.1	1.6	4.64	25.1	10.4	16.2
07/15/2002	9.00	1.5	5.4	5.20	25.5	14.0	14.6
07/17/2002	7.00	7.5	13.5	4.49	25.6	12.1	16.3
10/21/2003	7.00	3.2	19.4	4.51	29.4	12.4	20.7
10/23/2003	7.50	0.1	4.3	4.51	24.4	13.2	14.9
10/26/2003	10.00	0.6	4.5	4.78	24.9	14.0	15.5
10/28/2003	9.50	1.0	10.1	4.46	25.0	14.3	12.9
10/30/2003	6.00	5.0	13.5	4.47	26.7	12.9	17.2
11/01/2003	4.00	0.8	3.2	4.94	23.4	11.1	15.3
Mean	6.90	2.9	10.5	4.44	26.1	12.5	16.3

[*Chimonas*, 1986; *Lombard and Riley*, 1996; *Sonmor and Klaassen*, 1997] (for a complete discussion of gravity wave instability dynamics, see the review by *Fritts and Alexander* [2003] and the references therein). The traditional approaches, however, agree well with many observational studies in the mesopause region [*Hecht et al.*, 1997; *Williams et al.*, 2002; Li et al., submitted manuscript, 2004]. In this paper, we will use $N^2 < 0$ and $0 < Ri < 1/4$ for convective and dynamical instability, respectively, but the readers should keep in mind that these conditions are only highly suggestive of instabilities.

[8] Convective instability is determined solely from temperature profiles, whereas dynamical instability is characterized using both wind and temperature observations. Temperature is measured in every lidar beam position, which has a temporal resolution of ~2 min. Horizontal wind profiles, however, are only obtained in off-zenith positions. A complete ZNEZSW cycle includes six temperature profiles, two zonal wind profiles, and two meridional wind profiles. Therefore temperature has a higher temporal resolution than horizontal winds. The raw lidar data were binned to a resolution of 480 m along the LOS. When projected to the vertical, the off-zenith profiles have a vertical resolution of ~420 m. In order to reduce measurement uncertainties and calculate N^2 and Ri in a consistent way, the profiles need to be vertically and temporally smoothed.

[9] Errors in the calculation of N^2 are primarily due to uncertainties in temperature measurements, which are dominated by photon noise. Because the off-zenith LOS wind has a vertical component, uncertainties in the horizontal winds consist of photon noise and vertical wind contamination. The measurement uncertainties, along with the fact that u and v are sampled at different locations, are the main error sources in Ri. It is obvious that the values of N^2 and Ri, and hence the probability of instability, are sensitive to the vertical and temporal smoothing. Stronger smoothing reduces the vertical gradient, leading to larger values of N^2 when dT/dz is negative, and smaller values of S. As a result, unstable regions calculated using a weaker smoothing scheme may become stable when using stronger smoothing. There is no simple answer to what is the right scheme to be used. We have considered the following principles when designing the smoothing algorithm: (1) High vertical resolution is essential for detecting thin unstable layers; (2) The zonal and meridional winds are sampled at different locations and both are measured twice in opposite directions with respect to the zenith in one cycle which takes ~12 min. Assuming that the vertical wind does not change, averaging over at least one cycle would reduce the contamination of vertical wind on horizontal winds, because, for example, $u'_E + u'_W = u_E + u_W$. The smoothed wind can approximately represent the averaged value of the atmospheric volume between the off-zenith beams; and (3) Temperature and winds have the same resolution such that N^2, S, and Ri are calculated in a consistent manner. With these considerations in mind, the vertical smoothing is conducted by applying a Hamming window with a width of 1 km to all profiles at every 0.5 km. The 1 km Hamming window and 0.5 km vertical resolution were chosen to retain the high resolution of the raw data. Temporal smoothing is performed by binning the vertically smoothed profiles with a 15 min resolution. Totally, ~500 smoothed profiles of temperature and winds are obtained. N^2, S, and Ri are then calculated using the smoothed profiles, with vertical gradients of temperature and horizontal winds (dT/dz, du/dz, and dv/dz) computed using a center difference scheme with a spacing of 1 km. Average uncertainties for temperature and horizontal winds are 0.8 K and 2 ms^{-1} at the center of the Na layer (~92.5 km), and they increase to 1.5 K and 5 ms^{-1} at the edge of the Na layer (~85 and 100 km). Measurement uncertainties increase sharply below 85 km and above 100 km. Only the observations between 85 and 100 km are discussed in this paper.

3. Results

3.1. Statistics of Instabilities

[10] Probabilities of convective and dynamical instabilities for the 19 nights are summarized in Table 1. The instability probability on one night is calculated as the

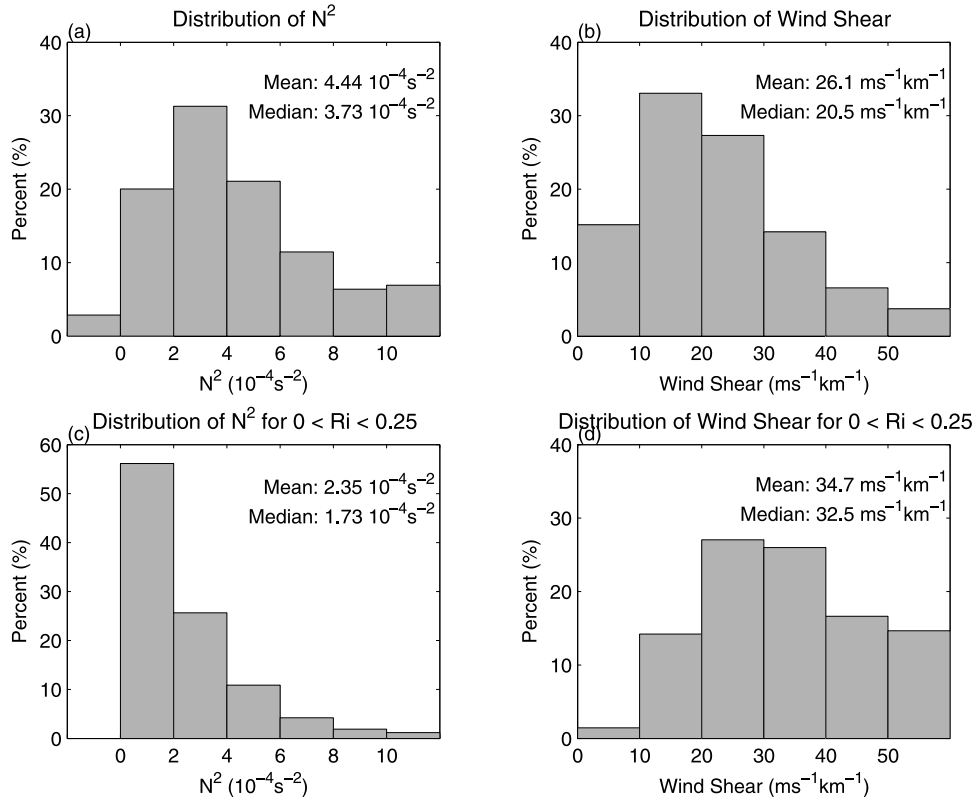

Figure 1. Histograms of (a) N^2, (b) amplitude of wind shear, (c) N^2 for $0 < Ri < 0.25$, and (d) amplitude of wind shear for $0 < Ri < 0.25$. Totally, 19 nights, ~133 hours of measurements are used to calculate the distributions of N^2 and wind shear.

percentage of the number of points whose N^2 is negative for convective instability, and whose Ri falls in the range of $0 < Ri < 0.25$ for dynamical instability to the total data set in the 85–100 km height range for the entire night. The mean probabilities of the 19 nights are 2.9% and 10.5% for convective and dynamical instability, respectively. Considerable night to night variations are found. The highest probability of convective instability occurs on the night of 22 January 2004 with a 10.7% percentage, whereas 23 October 2003 has the lowest probability of 0.1%. In terms of dynamical instability, the most unstable night is 15 April 2002 with a probability of 25.4%, and the most stable night is 13 July 2002 with a 1.6% probability. Generally, dynamical instability has a much larger probability to occur than convective instability. The only exceptions are the nights of 22 January 2004 and 13 July 2003 when probability of convective instability slightly exceeds that of dynamical instability. It should be pointed out that, at any give time, the probability of an unstable condition ($Ri < 0.25$) to be found at some altitude in the 85–100 km height range is 88%. That is, instability is almost always present at some altitudes at a given time.

[11] Also listed in Table 1 are the nightly and total mean values of N^2, S, $|du/dz|$ and $|dv/dz|$. The mean N^2 for all the nights is $4.44 \times 10^{-4}s^{-2}$. It should be noted that the standard deviation of N^2 is large with a value of $3.44 \times 10^{-4}s^{-2}$, which implies that the existence of large temperature gradients, both negative and positive, is common in the mesopause region. Given a mean N^2 of $4.44 \times 10^{-4}s^{-2}$, a wind shear stronger than 42 $ms^{-1}km^{-1}$ is required for the onset of a dynamical instability. This is much larger than the observed mean wind shear of 26.1 $ms^{-1}km^{-1}$. Therefore the mesopause atmosphere is, in general, dynamically stable, consistent with the calculated probability of dynamical instability. One interesting feature of the vertical shear in the horizontal winds is the dominance of $|dv/dz|$ over $|du/dz|$. On 17 out of the 19 nights, the nightly mean amplitude of the meridional wind shear is larger than that of the zonal wind shear. The total mean amplitude of the meridional wind shear is ~30% larger than that of the zonal wind shear. The possible physical processes underlying this phenomenon will be discussed in Section 4.

[12] The histogram of N^2 for all the 19 nights' data is shown in Figure 1a. The range of 2 to $4 \times 10^{-4}s^{-2}$ has the largest percentage, accounting for nearly 1/3 of the data. The percentage decreases almost consistently for $N^2 > 4 \times 10^{-4}s^{-2}$ and $N^2 < 2 \times 10^{-4}s^{-2}$. Of particular interest is the distribution of the reduced and enhanced N^2. Dynamical instability is more likely to occur when the atmosphere static stability is reduced. However, large N^2 is often observed to be associated with mesosphere inversion layers (MILs), a ubiquitous mesopause phenomenon whose generation mechanisms are unclear. Given a mean of $4.44 \times 10^{-4}s^{-2}$ and a standard deviation of $3.44 \times 10^{-4}s^{-2}$, hereafter we refer large (small) N^2 to those with values $>8 \times 10^{-4}s^{-2}$ (in the range of 0 and $1 \times 10^{-4}s^{-2}$). It is found that large N^2 consists of ~13.5%, and small N^2 ~6.7% of the data. Figure 1b shows the distribution of the amplitude of the vertical shear in the horizontal winds.

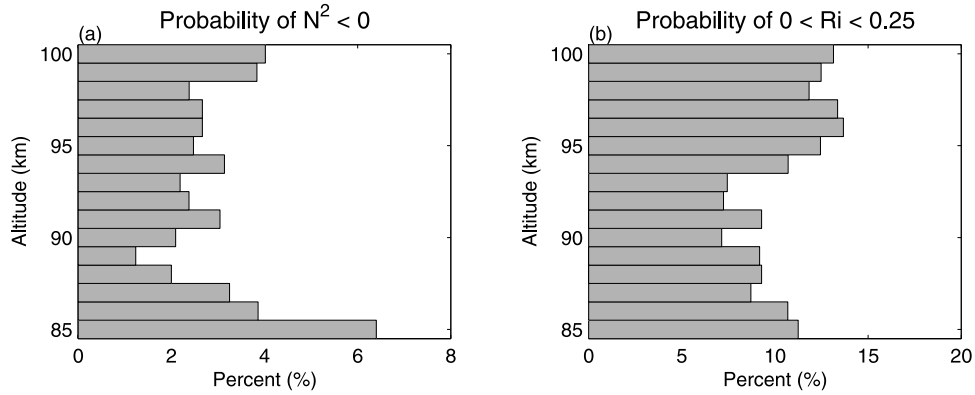

Figure 2. Histograms of (a) probability of convective instability as a function of altitude and (b) probability of dynamical instability as a function of altitude.

Nearly half of the wind shear has a magnitude smaller than 20 $ms^{-1}km^{-1}$, and only ~10% have wind shear larger than 40 $ms^{-1}km^{-1}$. Note that a wind shear of 40 $ms^{-1}km^{-1}$ has been used by several researchers as a nominal value for dynamical instability because the mean N^2 is $\sim 4 \times 10^{-4}s^{-2}$ in the mesopause region [*Hirota et al.*, 1983; *Taylor and Hapgood*, 1990].

[13] Although the percentage of large wind shear (>40 $ms^{-1}km^{-1}$) and the probability of dynamical instability are both ~10%, it turns out that this is just a coincidence. This is because the dynamical instability condition is related to both wind shear and vertical temperature gradient. This is further illustrated by the histograms of N^2 and wind shear for $0 < Ri < 0.25$, shown in Figures 1c and 1d. Very different distributions of N^2 and wind shear are found for dynamical instability conditions. Distribution of N^2 is shifted toward small values. The mean and median values decrease to about half the values of those when all data are considered. More than 50% of N^2 is within the range between 0 and $2 \times 10^{-4}s^{-2}$. The percentage of small N^2 increases to 32%, whereas the percentage of larger N^2 decreases to only 3%. Comparing Figure 1d with Figure 1b shows that the wind shear distribution shifts toward large value in dynamically unstable regions. The mean and median values both increase significantly. The percentage of large wind shear (>40 $ms^{-1}km^{-1}$) increases to 31%. It is clear that the dynamical instability, in a statistical sense, is a result of the combination of reduced static stability and enhanced wind shear.

[14] Distribution of instabilities as a function of altitude is presented in Figure 2. Figure 2a shows that the probability of convective instability decreases sharply from 85 to 89 km, and remains almost constant above 90 km with a small increase at 99 and 100 km altitude. The distribution of dynamical instability has a different structure (Figure 2b). The probability of dynamical instability decreases almost consistently above 85 km, reaching a minimum around 92 km, then increases rapidly with altitude to 96 km, and remains almost constant above. It is clearly seen from Figure 2b that dynamical instability is more likely to occur in the upper mesopause region (93–100 km) than in the lower region (85–93 km). This feature is not observed in the convective instability.

[15] In order to further investigate the vertical distribution of the instabilities, we plot profiles of mean N^2, mean horizontal wind shear S, and mean N^2/S^2 in Figure 3. The mean profile is calculated as the mean of the total ~500 profiles. The mean N^2 profile resembles an "S" shape with maxima at ~89 and 100 km and minima at ~85 and 96 km. There is not much correlation between the probability of convective instability and the mean value of N^2 except in the 85–89 km range, where the increase of static instability is consistent with the decrease of the probability of convective instability. Convective instability is more readily to occur when the background static stability is reduced because gravity wave induced temperature perturbations, when combined with small mean static stability, can more easily generate a superadiabatic lapse rate. However, the vertical distribution of the probability of convective instability above 90 km does not agree with that of the mean N^2 value, suggesting complicated nature of convective instability. Physical processes, such as gravity wave breaking and dissipation in the lower region, generation of shear instability, could affect the distribution of convective instability.

[16] The vertical profile of S (Figure 3b) has some similarities to those of the mean N^2, e.g., maxima at ~89 and 100 km and minima at ~85 and 96 km. S has another maximum at ~94 km and minimum at ~92.5 km. In addition, S exhibits a tendency of stronger wind shear with increasing altitude. The correlation coefficient between S and N^2 with the linear trend removed is 0.67, suggesting some correlation between the amplitude of wind shear and atmospheric static stability. Figure 3c shows the ratio of mean N^2 and mean S^2. It is found that the vertical distribution of the dynamical instability probability agrees well with that of N^2/S^2. We have shown that the probability of dynamical instability is larger above ~93 km than below. Figure 3c clearly shows a smaller mean N^2/S^2 above ~93 km than that below. It appears, by comparing Figures 3 and Figure 2b, that the tendency for wind shear increasing with altitude is mainly responsible for the enhanced probability of dynamical instability in the upper regions. There exists a transition region between ~92.5 and 94.5 km where N^2/S^2 decrease sharply from ~1.1 to 0.7, corresponding to the increase of dynamical instability probability at about the same region. Comparing Figures 3a and 3b reveals that this

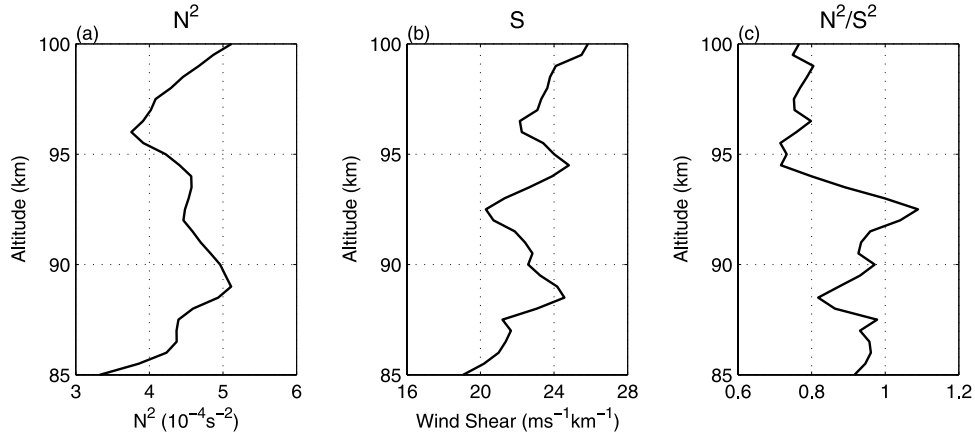

Figure 3. Vertical profiles of (a) mean N^2, (b) mean amplitude of wind shear S, and (c) mean N^2/S^2. The mean is calculated using all the Maui MALT data.

sharp transition region is caused by a large increase in the wind shear which is accompanied by nearly constant N^2.

3.2. Structure of Instabilities

[17] We have shown that the vertical variations of N^2 and wind shear appear to be related. Correlations between N^2 and wind shear are clearly seen in Figure 4a, which shows the histogram of wind shear as a function of N^2. Each bin represents the mean wind shear in regions where N^2 is within that specific range. Except for $N^2 < 0$, there is a trend of stronger wind shear with larger N^2. We found that the mean wind shear for large N^2 ($>8 \times 10^{-4}s^{-2}$) is nearly twice the magnitude of that for small N^2 ($<1 \times 10^{-4}s^{-2}$), indicating significant wind shear increase with increasing atmospheric static stability. A similar feature is observed in the distribution of the large wind shear (Figure 4b). Except for $N^2 < 0$, the relative percentage of the occurrence of strong wind shear

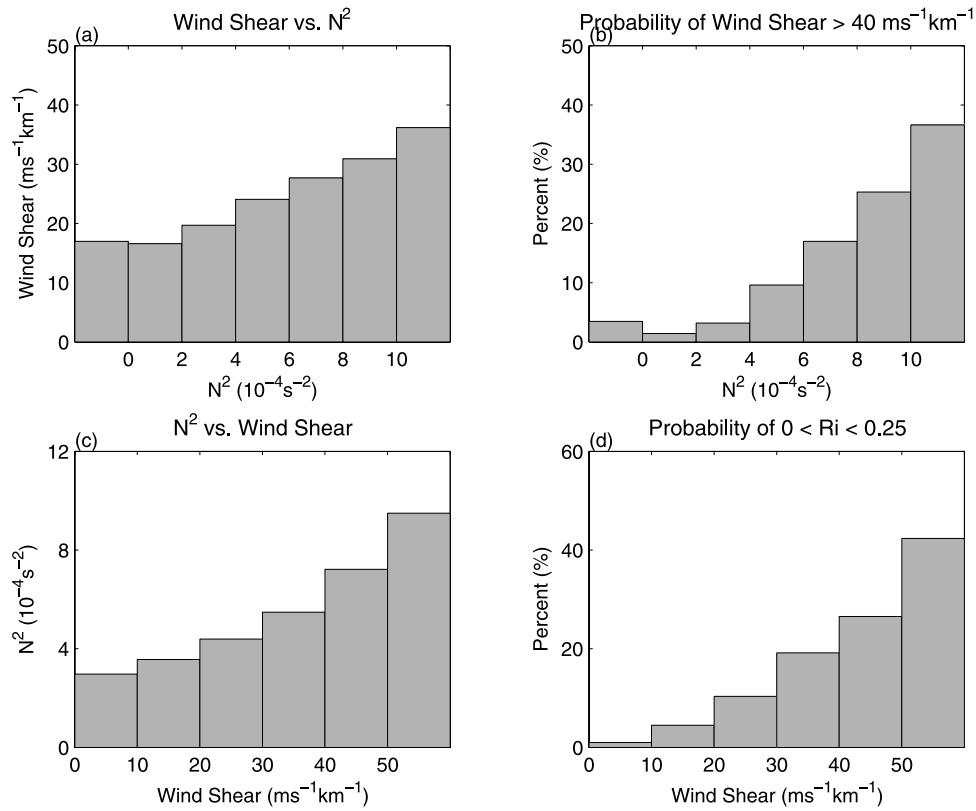

Figure 4. Histograms of (a) amplitude of wind shear as a function of N^2, (b) probability of the occurrence of large wind shear (>40 ms^{-1}km^{-1}) as a function of N^2, (c) N^2 as a function of wind shear, and (d) probability of dynamical instability as a function of wind shear amplitude. In Figures 4b and 4d the probability is relative to the corresponding data range.

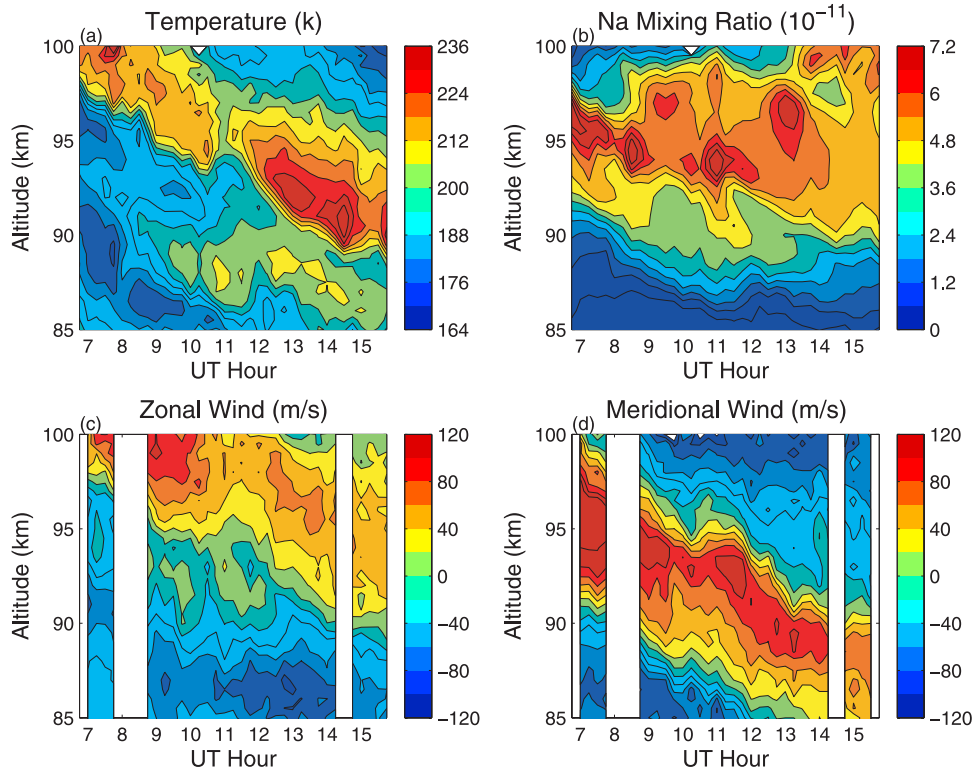

Figure 5. Time-height contour plots of (a) the temperature, (b) the Na mixing ratio, (c) the zonal wind, and (d) the meridional wind on the night of 11 April 2002.

(>40 $ms^{-1}km^{-1}$) increases sharply with N^2. Comparing with a 3% for $N^2 < 1 \times 10^{-4}s^{-2}$, a 30% of strong wind shear occurrence for $N^2 > 8 \times 10^{-4}s^{-2}$ suggests a physical linkage between strong wind shear and large N^2. Figure 4c presents the distribution of N^2 as a function of wind shear. Similar to that shown in Figure 4a, a tendency for N^2 increasing with wind shear is clearly seen. In summary, the Maui MALT data demonstrate consistent correlations between N^2 and wind shear, with a tendency for N^2 increasing with wind shear, and vice versa.

[18] Because dynamical instability is determined by both N^2 and wind shear, this relation between N^2 and wind shear has important implications to the distribution of dynamical instability. Figure 4d shows the relative percentage of dynamical instability as a function of total wind shear, which demonstrates clearly that dynamical instability is more likely to occur with strong wind shear. This is consistent with the findings noted in the previous section that dynamical instability is usually generated with small N^2 and large wind shear. It should be noted that the probability of dynamical instability for wind shear >40 $ms^{-1}km^{-1}$ (including the right two bins in Figure 4d) is ~35%. That is, nearly 2/3 of those points with wind shear >40 $ms^{-1}km^{-1}$ are dynamically stable. Because of the systematic correlations of wind shear with N^2, strong wind shear does not necessarily lead to Ri < 0.25. However, large N^2 does not guarantee dynamical stability since it always associated with strong wind shear.

[19] In order to better understand the spatial and temporal structures of N^2, wind shear, and instabilities, we study in detail the night of 11 April 2002. This night is chosen because it has all the characteristics discussed above and a long observation time of ~9 hours. Figure 5 shows the contour plots of temperature, zonal and meridional winds, and Na mixing ratio on this night. A strong temperature inversion layer, which descends from ~100 km at 0700 UT to ~90 km at 1600 UT, is the most significant feature in temperature. The amplitude of the inversion layer, which is defined as the difference between the maximum and minimum temperature, exceeds 30 K during most of the night. There exists another inversion layer at lower altitudes, with a weaker amplitude, between ~0700 and 1100 UT. The downward phase progression speed, ~1 km/hour, is consistent with the phase speed of the migrating diurnal tide [*Forbes*, 1995]. Horizontal winds also exhibit downward progression structures with similar phase speed. The wind speed is large with maximum values exceeding 100 ms^{-1}. Large vertical gradients of horizontal winds are found, especially in the meridional wind. Overturning in the Na mixing ratio, which indicates reverse in potential temperature gradient and convective instability, is observed throughout the night. The most significant overturning structure is found in the ~96–100 km height range between 1300 and 1500 UT.

[20] The spatial and temporal relations between convectively and dynamically unstable regions are illustrated in Figure 6. Most of the regions of small atmospheric static stability ($N^2 < 1 \times 10^{-4}s^{-2}$) are located just above the major inversion layer where temperature decreases sharply with altitude (Figure 6a). Reduced static stability is also found above and below the weaker inversion layer, and is limited to before 1100 UT. As the inversion layers descend with time, small N^2 regions also progress downward. Convective instability ($N^2 < 0$) is scattered within the small

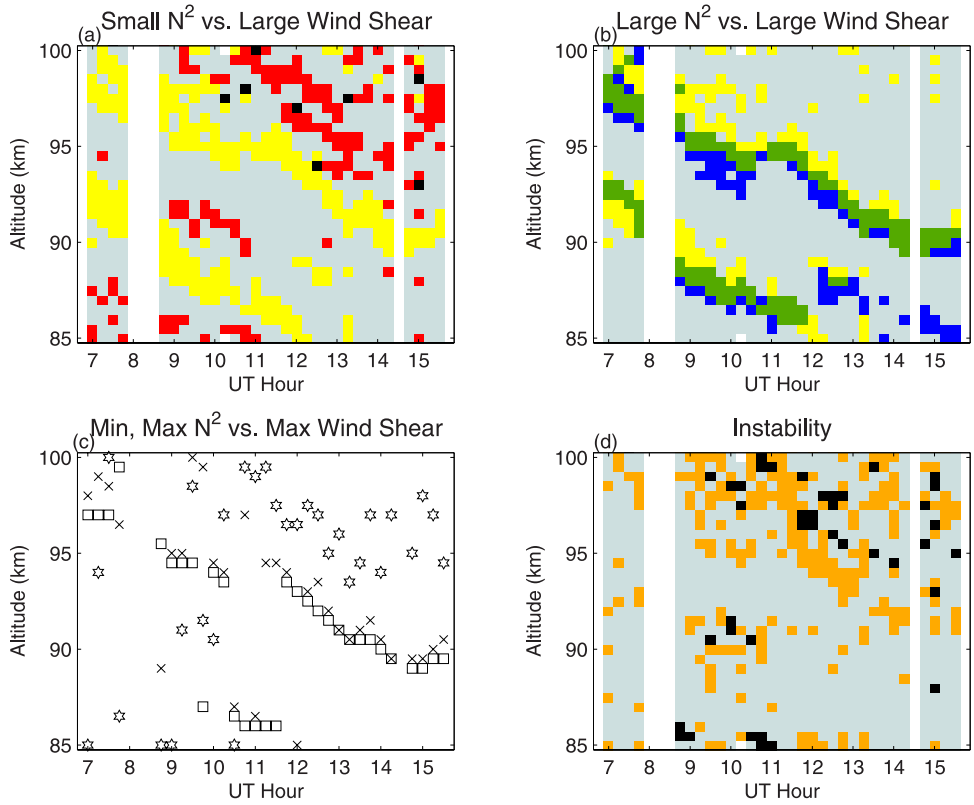

Figure 6. (a) Distributions of high wind shear and reduced static stability on the night of 11 April 2002. Yellow regions indicate large wind shear with amplitude >40 $ms^{-1}km^{-1}$, and red regions denote reduced static stability with $N^2 < 1 \times 10^{-4}$ s^{-2}. Areas where large wind shear overlaps small N^2 are indicated by black. Gray areas indicate neither large wind shear nor small N^2, and white areas have no data. (b) Same as Figure 6a, but blue regions indicate $N^2 > 8 \times 10^{-4}s^{-2}$, and green regions denote overlap of high wind shear with large N^2. Gray areas indicate neither large wind shear nor large N^2. (c) Locations of maximum wind shear amplitude (cross), maximum N^2 (square), and minimum N^2 (hexagram star). (d) Dynamically unstable regions are indicated by orange, whereas convectively unstable regions are indicated by black. Gray areas are stable.

N^2 regions (Figure 6d). Signatures of downward propagation of convective instability, which is associated with the progression of the upper inversion layer, can also be seen in Figure 6d.

[21] Large positive temperature gradients ($N^2 > 8 \times 10^{-4}s^{-2}$) are found just below the maxima of the inversion layers (Figure 6b, yellow plus green). Figure 6b shows two shallow layers of high static stability, with a width of 1–2 km, which descend with the inversion layers. The most striking feature in Figure 6b, however, is the nearly overlap of the layers of large N^2 with the layers of strong wind shear (>40 $ms^{-1}km^{-1}$). However, Figure 6a shows that there is no overlap between strong wind shear and small N^2 except for a few scattered points. Figure 6b also shows that although largely overlapped, the strong wind shear layer is located on the top of the large N^2 layer. This structure is more readily recognized in Figure 6c, which compares the altitudes of maximum and minimum N^2, and maximum wind shear amplitude. Figure 6c shows that altitudes of maximum N^2 and maximum wind shear are highly correlated, with maximum wind shears often located ~0.5–1 km above maximum N^2. There is no direct correlation between minimum N^2 and maximum wind shear, but it appears that maximum wind shear occurs prior to and below minimum N^2, a feature also identified by Z03.

[22] The structures of N^2 and wind shear determine the distribution of dynamical instability. We have shown that dynamical instability generally occurs when wind shear is large and static stability is small. Figure 6d shows that regions of dynamical instability appear to be presented in regions of small N^2 rather than those of large wind shear. Most of the dynamically unstable areas are located above the major inversion layer. The rest of the unstable regions correspond to reduced static stability regions above and below the lower inversion layer. As has been discussed, large wind shear does not necessarily cause dynamical instability because it is always accompanied by large N^2. This is especially true for the lower strong wind shear layer.

[23] The characteristics revealed in Figure 6 are elaborated by investigating structures of N^2, wind shear, and instabilities at 1245 UT on this night. Profiles of temperature and horizontal winds are shown in Figure 7a. There exist a lower weak and an upper strong inversion layer, which are associated with large N^2 (Figure 7b). The

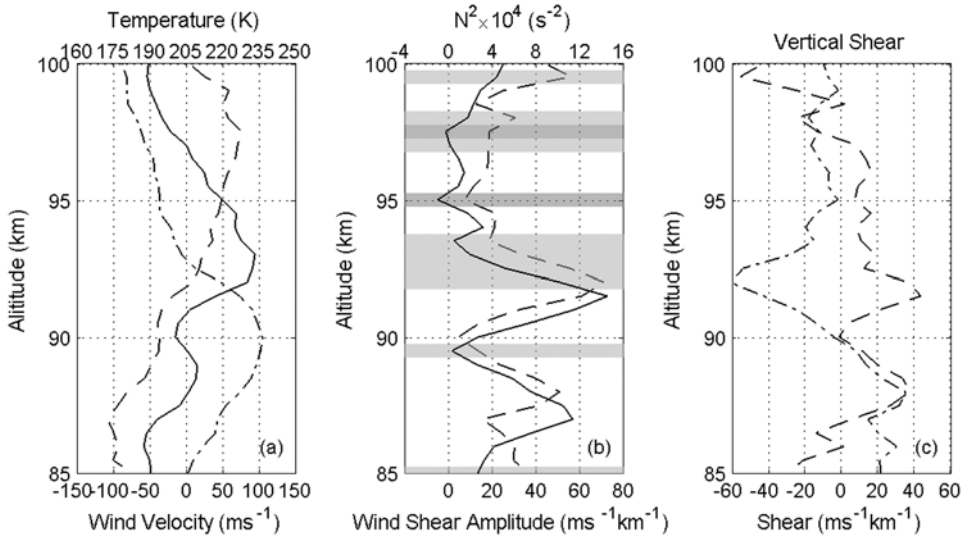

Figure 7. Profiles at 1245 UT, 11 April 2002. (a) Temperature (solid), zonal wind (dashed), and meridional wind (dash-dot). (b) N^2 (solid) and amplitude of the total wind shear (dashed). Shaded regions indicate convective instability (dark gray) and dynamical instability (light gray). (c) Vertical shear in the zonal wind (dashed) and meridional wind (dash-dot).

vertical variations of N^2 and wind shear amplitude are very similar, but with a phase shift (Figure 7b). The maxima and minima of wind shear are located $\sim$0.5–1 km above those of the N^2. This shift affects the locations of the dynamically unstable regions. The height range of 92–94 km is dynamically unstable. This region is above and includes the top of the upper strong wind shear layer, where the wind shear amplitude reaches its maximum and begins to decrease. Because of the phase shift of N^2 and wind shear, N^2 has already passed its maximum and starts decreasing where wind shear reaches its maximum, resulting a Ri value smaller than 0.25. Above the wind shear maximum, the decrease of N^2 leads the decrease of wind shear and Ri values <0.25 are still achieved. This dynamically unstable region ends where a N^2 minimum is reached. There are other dynamically unstable regions, some of which are associated with convective instability. Intuitively, Ri must enter the range of 0 to 0.25 before it becomes negative, although the resolution of the data may not be fine enough to discern this transition region. One example of this is the height range between 97 and 98.5 km where convective instability is sandwiched by dynamical instability. These two scenarios account for most of the situations where $0 < Ri < 0.25$ is observed. Since both scenarios occur above the inversion layer, this explains why dynamically unstable regions are primarily found above the inversion layers.

[24] The relative contributions of the zonal and meridional wind to the total wind shear are investigated in Figure 7c. The meridional wind shear has the same sign and almost the same amplitude as the zonal wind shear in the lower strong wind shear layer. However, the upper strong wind shear is dominated by the meridional wind shear, which has a magnitude $\sim$50% stronger than that of the zonal wind shear. The sign of the meridional wind shear changes to negative in the upper strong wind shear layer. It should be noted that the phase relationship between the gradients of temperature and wind is very different from the phase relationship between temperature and wind.

[25] Because tidal modulation is clearly seen in Figure 5, one question that needs to be answered is whether the observed features are simply caused by the tides alone. In order to answer the question, a comparison is made between Figure 5 and the tides from the Global-Scale Wave Model (GSWM) [*Hagan et al.*, 1999]. It is noted that, while the phase of the GSWM diurnal tidal winds agrees well with the phase of the observed winds, the phase and amplitude of the GSWM tidal temperature are very different from the observations (figure not shown). The phase relation between the GSWM tidal wind and temperature can not explain the observed correlation between wind and temperature gradients. The GSWM tidal temperature amplitude is $\sim$7 times smaller than the observed amplitude of temperature perturbations in the 90–95 km height range. Given that the GSWM results, especially the tidal phase, agree reasonably well with tides derived from satellite and ground-based measurements [*Hagan et al.*, 1999; *She et al.*, 2002], we conclude that tides alone can not explain the correlation, nor the particular structure of N^2 and wind shear shown in Figures 5–7. These observed features are likely to be related to the physical processes responsible for the inversion layer generation. Some of the processes will be discussed in the next section.

[26] It should be emphasized that the above reported characteristics of N^2, wind shear, and instabilities are not particular to the night of 11 April 2002. MILs are observed on each of the 19 nights. Most MILs exhibit downward progression structures. The correlation between N^2 and wind shear, including the phase shift and the dominance of the meridional wind shear, is commonly observed, though not on every night. The phase shift between N^2 and wind shear may not be exactly the same as that on the night of 11 April 2002, but the characteristics of the

distribution of instabilities are very similar to those shown in Figures 6 and 7.

4. Discussion

[27] The seasonal variability of instabilities is not investigated here because current Maui MALT data only cover 4 months which are insufficient for this kind of study. Comparison of the values of probability of instabilities between Maui and SOR is not performed, because different data analysis methods were used in this study and Z03. We employed the same data set (0.5 km, 15 min) to study both convective and dynamical instabilities. Z03, however, used different data sets to investigate convective and dynamical instabilities. In Z03, a higher resolution (0.5 km, 1.5 min) data set was used to study convective instability, whereas a lower resolution (1 km, 24 min) data set was used to assess dynamical instability. Despite the differences in the data analysis method, some similarities are found in the characteristics of instabilities between Maui and SOR. Both Z03 and this paper have found that thermal tides are important in modulating the background atmospheric stability and hence influence the occurrence of instabilities. The tendency for dynamical instability to develop before and below convective instability is observed in both SOR and Maui. This study clearly points out a linkage between MILs and instabilities, which is not investigated in Z03. Furthermore, we have shown in detail the correlation between N^2 and wind shear and its implications in the development of dynamical instability. Consequently, the relative locations of convective and dynamical instabilities cannot be simply explained by the phase difference in tidal temperature and winds. Instead, complex physical processes might be involved including, for example, gravity wave breaking and gravity wave-tidal interactions.

[28] It is not surprising to observe strong wind shear accompanying large N^2. In fact, this phenomenon can be explained by various different mechanisms involving gravity waves. Some of the mechanisms have been proposed to explain the generation of MILs [*Meriwether and Gardner*, 2000]. *Huang et al.* [1998, 2002] found large wind shear accompanying a mesopause MIL over Maui, HI during the ALOHA-93 campaign. They demonstrated that the large wind shear was related to a downward propagating gravity wave, and used this observation as a basis to argue that the inversion layer was due to gravity wave-mean flow, a critical layer interaction. When a gravity wave breaks in the critical level, it deposits momentum and energy into the mean flow, and increases the wind shear in the direction of wave propagation. In the case of a strong wave-mean flow interaction, dynamical instability might be generated. They argued that dissipation of kinetic energy of the mean flow in the dynamically unstable region cause the temperature rise and the MIL generation. A similar mechanism, but with different nature, was proposed by *Liu and Hagan* [1998] and *Liu et al.* [1999, 2000]. Using a 2-D model, they showed that interactions of gravity waves and tide-modulated mean flow can generate temperature inversion layers with characteristics similar to observations. A gravity wave may break via convective instability due to dynamical cooling when the gravity wave approaches its critical level. The breaking causes increased wind shear which may lead to shear instability below the breaking level. Downward heat flux which is generated by the breaking wave is enhanced by turbulence in the dynamically unstable region. As a result, the maximum heating altitude corresponds to regions of strong wind shear.

[29] Both theories are qualitatively consistent with the Maui MALT observations. Figures 6 and 7 show that there is a tendency for dynamical instability to develop below convective instability, especially when associated with the downward progression of tides. This feature appears to support the gravity wave-tidal interaction mechanism presented by *Liu and Hagan* [1998]. However, since gravity wave breaking and instabilities are inherently 3-D processes, 3-D numerical simulations with more realistic background conditions and gravity wave sources are needed to explain the observed structures.

[30] Wind shear induced by gravity wave could contribute significantly to the total wind shear. A decrease of the vertical wavelength of a gravity wave can lead to significant increase of the wind shear induced by the gravity wave. The linear gravity wave dispersion relation is

$$m^2 = \frac{N^2}{(C_O - U)^2} - k^2 - \frac{1}{4H^2}, \tag{5}$$

where m is the vertical wave number, C_o is the observed phase speed, U is the background wind, k is the horizontal wave number, and H is the density scale height. The vertical wavelength will decrease sharply in a region where N^2 increases sharply. Figure 7b shows that N^2 can increase up to 10 times in a narrow range of $\sim$2 km. Such sharp increase of N^2 is commonly observed accompanying MILs over Maui, HI. Therefore an increase of wind shear induced by gravity waves with large N^2 is consistent with the observations. It is most likely that this process, which is combined with the mechanisms discussed above, generates the strong correlation between large N^2 and strong wind shear.

[31] We have noticed that vertical shear in the meridional wind is larger than that in the zonal wind. To further investigate this feature, the azimuth distribution of wind shear vectors is presented in Figure 8. Figure 8a shows the percentages of wind shear vectors falling in one of the octants, regardless of their amplitudes. There is a small bias in the meridional directions, with slightly larger percentages toward the north and south than toward the east and west. The preference of wind shear occurring in the meridional directions, especially toward the south, becomes much more significant when only dynamically unstable regions (Figure 8b) or wind shear amplitude larger than 40 $ms^{-1}km^{-1}$ (Figure 8c) are considered. It is also found that the negative meridional wind shear often occurs in the upper mesopause region, and the positive meridional wind shear is usually located in the lower mesopause region, which is apparently related to the phase of the diurnal tide at night. As illustrated in Figure 7c, the upper negative meridional wind shear always has a larger magnitude than the lower positive meridional wind shear, which might explain the larger percentage of wind shear toward the south than toward the north.

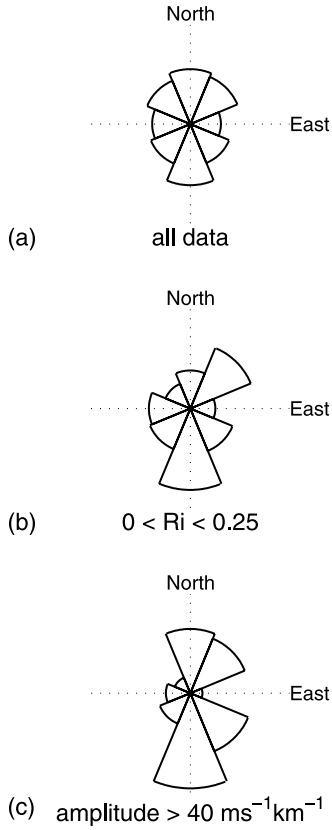

Figure 8. Azimuth distribution of wind shear vectors for (a) all data, (b) $0 < Ri < 0.25$, and (c) wind shear > 40 ms^{-1}km^{-1}.

[32] Similar structures, including the correlation of strong wind shear with temperature maximum and significantly stronger vertical shear in the meridional wind than in the zonal wind, were found accompanying the majority of the sporadic Na layers during the ALOHA-93 campaign [*Qian et al.*, 1998]. *Qian et al.* [1998] proposed that the correlation of strong wind shear with enhanced temperature might be caused by large-amplitude short-vertical wavelength gravity waves. According to the linear gravity wave theory, gravity wave temperature perturbation is in phase with the vertical shear of horizontal wind perturbation, so the phase relationship is consistent with their observations. However, we do not believe a large-amplitude gravity wave alone can explain the observed correlation between wind shear and temperature gradient in the Maui MALT data, nor can it generate a wind shear as large as 40 ms^{-1}km^{-1}. First of all, the correlation we identified is between wind shear and temperature gradient, which, according to the linear gravity wave theory, should be 90° out of phase. Theoretically, a large-amplitude short-vertical wavelength gravity wave can generate >40 ms^{-1}km^{-1} wind shear, e.g., *Qian et al.* [1998] argued that their observed 42 ms^{-1}km^{-1} wind shear was due to a gravity wave with a vertical wavelength of 4 km and a horizontal wind amplitude of 27 ms^{-1}. There is no observational evidence, however, to support the common presence of this kind of wave. *Hu et al.* [2002] characterized ~700 monochromatic gravity waves using ~300 hours of simultaneous wind and temperature profiles obtained with the University of Illinois Na lidar system at Starfire Optical Range, NM (35°N, 106.5°W). They found that the mean vertical wavelength is ~12 km. The percentage of gravity waves with vertical wavelength <5 km is less than 1%. *Collins and Smith* [2004] obtained statistically significant measurements of 24 upward propagating gravity waves during 4-year period lidar observations at Poker Flat Research Range, Chatanika, Alaska (65°N, 147°W). The mean characteristics of the 24 gravity waves include vertical wavelength of 14.2 km, temperature amplitude of 8 K, and horizontal velocity amplitude of 30 ms^{-1}. Of the 24 waves, none has a vertical wavelength <4 km. These observations suggest that, only in very exceptional case can a gravity wave with large-amplitude and short-vertical wavelength induce a wind shear as large as 40 ms^{-1}km^{-1}. It should be also pointed out that short-vertical wavelength waves are subject to heavy viscous dissipation [*Hecht et al.*, 2001]. For a nominal atmospheric kinematic viscosity of 300 m^{2}s^{-1}, the timescale for wave dissipation is ~45 min when the vertical wavelength is 4 km. This is not consistent with the observations of strong wind shear layer throughout the entire night (Figure 5). In summary, it is not likely, given the large magnitude of the wind shear and temperature gradient, that a gravity wave alone without wave-wave, wave-mean flow/tidal interactions can generate the observed structure.

[33] Because strong wind shear could be an indication of strong gravity wave-mean flow interactions, the dominance of meridional wind shear might imply that gravity waves in the mesopause region propagate preferentially in the meridional directions. In fact, numerous mesopause airglow studies have revealed that the propagation direction of the quasi-monochromatic high-frequency gravity waves is preferentially in the meridional, but with a seasonal variation [e.g., *Walterscheid et al.*, 1999; *Hecht et al.*, 2001; *Nakamura et al.*, 2001; *Tang et al.*, 2002]. The high-frequency waves have a tendency to propagate toward the summer pole, i.e., toward north in boreal summer and south in boreal winter. The same trend is found over Maui, HI [*Tang et al.*, 2005]. It is likely there is a linkage between the directionality of the wind shear and high-frequency gravity wave propagation. However, current Maui MALT lidar wind data are insufficient for a seasonal variability study.

5. Summary

[34] The mean probabilities of convective and dynamical instabilities in the mesopause region over Maui, HI are, respectively, ~3% and 10%, but there is considerable night-to-night variation. At any given time, the probability that an unstable condition ($Ri < 0.25$) is found at some altitudes in the 85–100 km range is ~90%. The vertical distributions of the mean probabilities of convective and dynamical instabilities exhibit different structures. The mean probability of dynamical instability is larger above ~93 km than below, which is attributed to a trend for wind shear increasing with altitude. This structure, however, is not observed in the probability of convective instability.

[35] We report, for the first time in a statistical manner, a correlation between N^2 and wind shear in the mesopause region. The Maui MALT data exhibit a distinct trend for N^2 to increase with wind shear, and vice versa. The correlation

between N^2 and wind shear has important implications in the development of instability. It is generally true that dynamical instability occurs with small N^2 and large wind shear. However, due to the correlation, strong wind shear does not necessarily lead to unstable conditions. Therefore cautions must be taken when assuming a critical wind shear limit of 40 $ms^{-1}km^{-1}$ for dynamical instability. However, large N^2 is likely related to dynamical instability due to large wind shear associated with reduced vertical wavelength of gravity waves. Because the magnitude of N^2 and wind shear can change significantly in a very short range, high-resolution wind and temperature measurements are essential for instability study.

[36] A close linkage between instabilities and MILs is identified. Most of the convectively and dynamically unstable areas are located above the MILs, with a tendency for dynamical instability to develop below convective instability. This particular structure is closely related to the correlation between N^2 and wind shear. It is found that the vertical variations of N^2 are often correlated with those of wind shear, but with a phase shift such that the maxima and minima of N^2 are located $\sim$1 km below those of wind shear. This phase shift affects where dynamical instability occur. N^2 starts to decrease below the maximum wind shear. As a result, relatively small N^2 is associated with large wind shear in the region on the topside and above the strong wind shear layers, where dynamical instability tends to develop. Since this region is below N^2 minimum where convective instability usually occurs, the tendency for dynamical instability developing below convective instability is explained.

[37] Another interesting phenomenon revealed in the Maui MALT data is the dominance of the vertical shear in the meridional wind over that in the zonal wind, especially in the region of strong total wind shear. It is unknown in this stage what causes this phenomenon, although we have noticed it might be related to the directionality of gravity waves in the mesopause region.

[38] The structures of N^2, wind shear, and instabilities are apparently related to tides and gravity waves. Considering the large magnitude of wind shear and N^2, it is very unlikely that tides or gravity waves alone can generate such a strong signature in wind and temperature. It is more likely that interactions of gravity waves with tidal-modulated mean flow play a decisive role. It is clear, however, that more observational and numerical studies are needed to investigate the nature of how wave-mean flow interactions can generate the observed wind and temperature structures.

[39] **Acknowledgments.** This work has been supported by NSF grants ATM 0003 180 and ATM 00-338425 in support of the airglow and Na lidar observations and data analysis for the Maui MALT program. In addition, support from NASA NAG 5-13593 is acknowledged for support of data analysis and modeling. Support from the Air Force and Boeing personnel in the operations of the Maui Telescope facility is most appreciated.

References

Andreassen, O., C. E. Wasberg, D. C. Fritts, and J. R. Isler (1994), Gravity wave breaking in two and three dimensions: 1. Model description and comparison of two-dimensional evolutions, *J. Geophys. Res.*, *99*, 8095–8108.

Andreassen, O., P. O. Hvidsten, D. C. Fritts, and S. Arendt (1998), Vorticity dynamics in a breaking internal gravity wave. Part 1. Initial instability evolution, *J. Fluid Mech.*, *367*, 27–46.

Chimonas, G. (1986), The combined Rayleigh, Kelvin-Helmholtz problem, *Phys. Fluids*, *29*(7), 2061–2066.

Chu, X., C. S. Gardner, and S. J. Franke (2005), Nocturnal thermal structure of the MLT region at Maui, Hawaii (20.7°N), and Starfire Optical Range, New Mexico (35°N), *J. Geophys. Res.*, *110*, D09S03, doi:10.1029/2004JD004891.

Clemesha, B. R., D. M. Simonich, P. P. Batista, and V. W. J. H. Kirchhoff (1982), The diurnal variation of atmosphere sodium, *J. Geophys. Res.*, *87*, 181–186.

Collins, R. L., and R. W. Smith (2004), Evidence of damping and overturning of gravity waves in the Arctic mesosphere: Na lidar and OH temperature observations, *J. Atmos. Sol. Terr. Phys.*, *66*, 867–879.

Forbes, J. M. (1995), Tidal and planetary waves, in *The Upper Mesosphere and Lower Thermosphere: A Review of Experiment and Theory*, *Geophys. Monogr. Ser.*, vol. 87, edited by R. M. Johnson and T. L. Killeen, pp. 67–87, AGU, Washington, D. C.

Fritts, D. C., and M. J. Alexander (2003), Gravity wave dynamics and effects in the middle atmosphere, *Rev. Geophys.*, *41*(1), 1003, doi:10.1029/2001RG000106.

Fritts, D. C., and P. K. Rastogi (1985), Convective and dynamical instabilities due to gravity wave motions in the lower and middle atmosphere: Theory and observations, *Radio Sci.*, *20*, 1247–1277.

Fritts, D. C., and L. Yuan (1989), Stability analysis of inertia-gravity wave structure in the middle atmosphere, *J. Atmos. Sci.*, *46*, 1738–1745.

Fritts, D. C., J. R. Isler, and O. Andreassen (1994), Gravity wave breaking in two and three dimensions: 2, Three dimensional evolution of instability structure, *J. Geophys. Res.*, *99*, 8109–8123.

Fritts, D. C., J. R. Isler, J. H. Hecht, R. L. Walterscheid, and O. Andreassen (1997), Wave breaking signatures in sodium densities and OH nightglow: 2, Simulation of wave and instability structures, *J. Geophys. Res.*, *102*, 6669–6684.

Fritts, D. C., S. Ardndt, and O. Andreassen (1998), Vorticity dynamics in a breaking internal gravity wave. part 2. Vortex interactions and transition to turbulence, *J. Fluid Mech.*, *367*, 47–65.

Hagan, M. E., M. D. Burrage, J. M. Forbes, J. Hackney, W. J. Randel, and X. Zhang (1999), GSWM-98: Results from migrating solar tides, *J. Geophys. Res.*, *104*, 6813–6827.

Hecht, J. H. (2004), Instability layers and airglow imaging, *Rev. Geophys.*, *42*, RG1001, doi:10.1029/2003RG000131.

Hecht, J. H., R. L. Walterscheid, D. C. Fritts, J. R. Isler, D. C. Senft, C. S. Gardner, and S. J. Franke (1997), Wave breaking signatures in OH airglow and sodium densities and temperature: 1. Airglow imaging, Na lidar, and MF radar observations, *J. Geophys. Res.*, *102*, 6655–6668.

Hecht, J. H., R. L. Walterscheid, M. P. Hickey, and S. J. Franke (2001), Climatology and modeling of quasi-monochromatic atmospheric gravity waves observed over Urbana Illinois, *J. Geophys. Res.*, *106*, 5181–5195.

Hickey, M. P., and J. M. C. Plane (1995), A chemical-dynamical model of wave-driven sodium fluctuations, *Geophys. Res. Lett.*, *22*, 2861–2864.

Hirota, I., Y. Maekawa, S. Fukao, K. Fukuyama, M. P. Sulzer, J. L. Fellous, T. Tsuda, and S. Kato (1983), Fifteen-day observation of mesospheric and lower thermospheric motion with the aid of the Arecibo UHF radar, *J. Geophys. Res.*, *88*, 6835–6842.

Hodges, R. R., Jr. (1967), Generation of turbulence in the upper atmosphere by internal gravity waves, *J. Geophys. Res.*, *72*, 3455–3458.

Hu, X., A. Z. Liu, C. S. Gardner, and G. R. Swenson (2002), Characteristics of quasi-monochromatic gravity waves observed with Na lidar in the mesopause region at Starfire Optical Range, NM, *Geophys. Res. Lett.*, *29*(24), 2169, doi:10.1029/2002GL014975.

Huang, T. Y., H. Hur, T. F. Tuan, X. Li, E. M. Dewan, and R. H. Picard (1998), Sudden narrow temperature-inversion-layer formation in ALOHA-93 as a critical-layer-interaction phenomenon, *J. Geophys. Res.*, *103*, 6323–6332.

Huang, T. Y., M. P. Hickey, T. F. Tuan, E. M. Dewan, and R. H. Picard (2002), Further investigation of a mesospheric inversion layer observed in the ALOHA-93 campaign, *J. Geophys. Res.*, *107*(D19), 4408, doi:10.1029/2001JD001186.

Isler, J. R., D. C. Fritts, and O. Andreassen (1994), Gravity wave breaking in two and three dimensions: 3. Vortex breakdown and transition to isotropy, *J. Geophys. Res.*, *99*, 8125–8137.

LeLong, M.-P., and T. J. Dunkerton (1998a), Inertia-gravity wave breaking in three dimensions, 1, Convectively stable waves, *J. Atmos. Sci.*, *55*, 2473–2488.

LeLong, M.-P., and T. J. Dunkerton (1998b), Inertia-gravity wave breaking in three dimensions, 2, Convectively unstable waves, *J. Atmos. Sci.*, *55*, 2489–2501.

Lindzen, R. S. (1981), Turbulence and stress owing to gravity wave and tidal breakdown, *J. Geophys. Res.*, *86*, 9707–9714.

Liu, A. Z., R. G. Roble, J. H. Hecht, M. F. Larsen, and C. S. Gardner (2004), Unstable layers in the mesopause region observed with Na lidar

during the Turbulent Oxygen Mixing Experiment (TOMEX) campaign, *J. Geophys. Res.*, *109*, D02S02, doi:10.1029/2002JD003056.

Liu, H.-L., and M. E. Hagan (1998), Local heating/cooling of the mesosphere due to gravity wave and tidal coupling, *Geophys. Res. Lett.*, *25*, 2941–2944.

Liu, H.-L., P. B. Hays, and R. G. Roble (1999), A numerical study of gravity wave breaking and impacts on turbulence and mean state, *J. Atmos. Sci.*, *56*, 2152–2177.

Liu, H.-L., M. E. Hagan, and R. G. Roble (2000), Local mean state change due to gravity wave breaking modulated by the diurnal tide, *J. Geophys. Res.*, *105*, 12,381–12,396.

Lombard, P. N., and J. J. Riley (1996), Instability and breakdown of internal gravity waves. 1. Linear stability analysis, *Phys. Fluids*, *8*, 3271–3287.

Meriwether, J. W., and C. S. Gardner (2000), A review of the mesosphere inversion layer phenomenon, *J. Geophys. Res.*, *105*, 12,405–12,416.

Miles, J. W. (1961), On the stability of heterogeneous shear flows, *J. Fluid Mech.*, *10*, 496–508.

Nakamura, T., A. Higashikawa, T. Tsuda, and Y. Matsushita (1999), Seasonal variations of gravity wave structures in OH airglow with a CCD imager at Shigaraki, *Earth Planets Space*, *51*, 897–906.

Nakamura, T., T. Tsuda, R. Maekawa, M. Tsutsumi, K. Shiokawa, and T. Ogawa (2001), Seasonal variation of gravity waves with various temporal scales in the MLT region observed with radar and airglow imaging, *Adv. Space Res.*, *27*, 1737–1742.

Qian, J., Y. Gu, and C. S. Gardner (1998), Characteristics of the sporadic Na layers observed during the Airborne Lidar and Observations of Hawaiian Airglow/Airborne Noctilucent Cloud (ALOHA/ANLC-93) campaign, *J. Geophys. Res.*, *103*, 6333–6348.

She, C. Y., S. Chen, B. P. Williams, Z. Hu, and D. A. Krueger (2002), Tides in the mesopause region over Fort Collins, Colorado (41°N, 105°W) based on lidar temperature observations covering full diurnal cycles, *J. Geophys. Res.*, *107*(D18), 4350, doi:10.1029/2001JD001189.

Sonmor, L. J., and G. P. Klaassen (1997), Toward a unified theory of gravity wave breaking, *J. Atmos. Sci.*, *54*, 2655–2680.

Swenson, G. R., and S. B. Mende (1994), OH emission and gravity waves (including a breaking wave) in all-sky imagery from Bear Lake, UT, *Geophys. Res. Lett.*, *21*, 2239–2242.

Tang, J., A. Z. Liu, and G. R. Swenson (2002), High frequency gravity waves observed in OH airglow at Starfire Optical Range, NM: Seasonal variations in momentum flux, *Geophys. Res. Lett.*, *29*(20), 1966, doi:10.1029/2002GL015794.

Tang, J., G. R. Swenson, A. Z. Liu, and F. Kamalabadi (2005), Observational investigations of high-frequency gravity wave momentum flux with airglow imaging, *J. Geophys. Res.*, doi:10.1029/2004JD004778, in press.

Taylor, M. J., and M. A. Hapgood (1990), On the origin of ripple-type wave structure in the OH nightglow emission, *Planet. Space Sci.*, *38*, 1421–1430.

Taylor, M. J., W. R. Pendleton Jr., S. Clark, H. Takahashi, D. Gobbi, and R. A. Goldberg (1997), Image measurements of short-period gravity waves at equatorial latitudes, *J. Geophys. Res.*, *102*, 26,283–26,299.

Walterscheid, R. L., J. H. Hecht, R. A. Vincent, I. M. Reid, J. Woithe, and M. P. Hickey (1999), Analysis and interpretation of airglow and radar observations of quasi-monochromatic gravity wave in the upper mesosphere and lower thermosphere over Adelaide (35°S, 138°E), *J. Terr. Sol. Atmos. Phys.*, *61*, 461–478.

Williams, B. P., M. A. White, D. A. Krueger, and C. Y. She (2002), Observation of a large amplitude wave and inversion layer leading to convective instability in the mesopause region over Fort Collins, CO (41°N, 105°W), *Geophys. Res. Lett.*, *29*(17), 1850, doi:10.1029/2001GL014514.

Yamada, Y., H. Fukunishi, T. Nakamura, and T. Tsuda (2001), Breaking of small–scale gravity wave and transition to turbulence observed in OH airglow, *Geophys. Res. Lett.*, *28*, 2153–2156.

Zhao, Y., A. Z. Liu, and C. S. Gardner (2003), Measurements of atmospheric stability in the mesopause region at Starfire Optical Range, NM, *J. Terr. Sol. Atmos. Phys.*, *65*, 219–232.

F. Li, Department of Atmospheric Sciences, University of Illinois at Urbana-Champaign, 1308 W. Main, Urbana, IL 61801, USA. (fengli@uiuc.edu)

A. Z. Liu and G. R. Swenson, Department of Electrical and Computer Engineering, University of Illinois at Urbana-Champaign, 1308 W. Main, Urbana, IL 61801, USA.